Quantum entanglement in polarization and space

Lee, Peter Sing Kin

CHAPTER 7

Polarization entanglement behind single-mode fibers: spatial selection and spectral labeling

We study the limitations to the polarization entanglement of photon pairs that are generated via type-II spontaneous parametric down-conversion (SPDC). By employing single-mode detection behind optical fibers, we demonstrate the incompleteness of the mode-matching concept presented in Ref. [23]. Using free-space detection behind apertures as well, we demonstrate that the higher entanglement quality obtained behind single-mode fibers is due to the removal of the spatial labeling. In addition, we show that the residual spectral labeling after selection with fibers is due to imperfect phase matching.

7.1 Introduction

Type-II spontaneous parametric down-conversion in a nonlinear birefringent crystal provides for a popular source of polarization-entangled twin photons in the field of experimental quantum optics and quantum information [8, 11, 15, 58]. In this generation process, one unavoidably encounters both longitudinal and transverse walk-off effects that are caused by the birefringent nature of the crystal. These make the polarizations of the twin photons distinguishable through their temporal and spatial information, respectively. This is also known as *labeling*. In order to restore the indistinguishability and thus the degree of polarization entanglement, Kwiat *et al.* [8] introduced a simple compensating device. It consists of one half-wave plate and two additional crystals, identical to the down-conversion crystal but of half the length. This device is now commonly used in several experimental schemes [23, 24, 56, 81].

The described compensating device is not perfect. With its frequency- and angle-dependent birefringence it can make the *phase* factors of the two contributing biphoton amplitude functions identical. The *amplitude* factors can however still be different, which implies that the obtained degree of polarization entanglement may still suffer from labeling, even when compensating crystals are used. In this chapter we study the limitations that spatial and spectral labeling impose on the attainable quality of the polarization entanglement.

Spatial labeling information, which is dosed by the detected angular width of the SPDC light, can be erased by transverse mode selection via single-mode fibers before photon detection. Kurtsiefer *et al.* [23] successfully pioneered this detection method to obtain both a large photon-pair collection and a high quality of polarization entanglement ($\approx 96\,\%$). However, the geometric requirement mentioned in Ref. [23], being the matching of pump and fiber mode, is not sufficient. We will show that an optimal yield of photon pairs needs extra matching with a third spatial parameter. Moreover, the benefit of fiber detection above the more conventional detection behind apertures was not highlighted in [23]. In this chapter we explicitly demonstrate that spatial labeling plays a crucial role in the comparison between these two schemes, especially in relation to the polarization entanglement quality. Furthermore, we show how pump beam properties can affect the entanglement measured behind single-mode fibers.

7.2 Theory

The theoretical description of polarization entanglement created under type-II SPDC can be found in Chapter 2. As a reminder, we mention that the polarization-entangled state at the intersections 1 and 2 of the two emitted SPDC light cones is given by the complete biphoton wavefunction [see also Eq. (2.7)]

$$|\Psi\rangle = \int d\mathbf{q}_1\, d\mathbf{q}_2\, d\omega_1\, d\omega_2\, \{\Phi_{HV}(\mathbf{q}_1,\omega_1;\mathbf{q}_2,\omega_2)\,|H_1,\mathbf{q}_2,\omega_1;V_2,\mathbf{q}_2,\omega_2\rangle + \Phi_{VH}(\mathbf{q}_1,\omega_1;\mathbf{q}_2,\omega_2)\,|V_1,\mathbf{q}_1,\omega_1;H_2,\mathbf{q}_2,\omega_2\rangle\}\,, \tag{7.1}$$

where integration is over the transverse wavevectors $\mathbf{q}_1$ and $\mathbf{q}_2$ and frequencies ω_1 and ω_2. The state $|H_1,\mathbf{q}_1,\omega_1;V_2,\mathbf{q}_2,\omega_2\rangle$ corresponds to the presence of one H-polarized photon with wavelength ω_1 and transverse wavevector $\mathbf{q}_1$ in beam 1 and its V-polarized partner

photon with wavelength ω_2 and transverse wavevector $\mathbf{q}_2$ in beam 2. A potential difference between the biphoton amplitude functions Φ_{HV} and Φ_{VH} is denoted as labeling and reduces the quality of the polarization entanglement. For free-space detection with bucket detectors behind apertures the degree of polarization entanglement is given by the biphoton visibility [see also Eq. (2.8)]

$$V = \frac{\langle\langle 2\mathrm{Re}(\Phi_{HV}^{*}\Phi_{VH})\rangle\rangle}{\langle\langle |\Phi_{HV}|^2 + |\Phi_{VH}|^2\rangle\rangle} \,. \tag{7.2}$$

The double brackets $\langle\langle\cdots\rangle\rangle$ denote the six-fold integration over the momenta $\mathbf{q}_1$ and $\mathbf{q}_2$ and frequencies ω_1 and ω_2, determined by the two spatial apertures and the transmission spectra of the two bandwidth filters, respectively.

In this chapter we also study the polarization entanglement observed behind *single-mode fibers* using fiber-coupled detectors [23, 56, 82]. In this case, the above equations remain basically the same; only the biphoton amplitude functions Φ_{ij} will change into the projected amplitude functions

$$\alpha_{ij}(\omega_1,\omega_2) = \int\int d\mathbf{q}_1\, d\mathbf{q}_2\; \Phi_{ij}\,(\mathbf{q}_1,\omega_1;\mathbf{q}_2,\omega_2)\; \psi^{*}_{\mathrm{fiber}\,1}(\mathbf{q}_1)\, \psi^{*}_{\mathrm{fiber}\,2}(\mathbf{q}_2)\,. \tag{7.3}$$

Here, $\psi_{\mathrm{fiber}\,1}(\mathbf{q}_1)$ and $\psi_{\mathrm{fiber}\,2}(\mathbf{q}_2)$ are the transverse mode profiles of the single-mode fibers in beam 1 and 2. Similar to Eq. (7.2), the degree of polarization entanglement can now be expressed as

$$V_{\mathrm{fiber}} = \frac{\langle 2\mathrm{Re}(\alpha_{HV}^{*}\alpha_{VH})\rangle}{\langle |\alpha_{HV}|^2 + |\alpha_{VH}|^2\rangle} \,, \tag{7.4}$$

where the single brackets denote a two-fold integration over the frequencies ω_1 and ω_2 only, over ranges determined by the transmission windows of the spectral filters in beam 1 and 2. It is obvious that Eq. (7.4) contains no spatial labeling information as the amplitude functions $\alpha_{ij}(\omega_1,\omega_2)$ depend only on frequency. In comparison with detection behind apertures, detection behind single-mode fibers should thus result in a higher degree of polarization entanglement. The sole limitation that can now potentially affect the polarization entanglement is spectral labeling.

7.3 Experimental results

7.3.1 Experimental setup

The experimental setup is schematically depicted in Fig. 7.1. Light from a cw krypton-ion laser, operating at 407 nm, is focused on a 1-mm-thick birefringent β-barium borate (BBO) crystal. The two cones of light that are emitted at 814 nm under type-II SPDC intersect each other perpendicularly, thereby defining two slightly diverging light paths which are both spaced at an angle of about 3° with respect to the pump beam. One half-wave plate and two 0.5-mm-thick BBO crystals (one in each arm) compensate for walk-off effects in the down-conversion crystal. After passing through apertures the light is imaged by a f = 40 cm lens, positioned at 80 cm from the down-conversion crystal, to an intermediate focus,

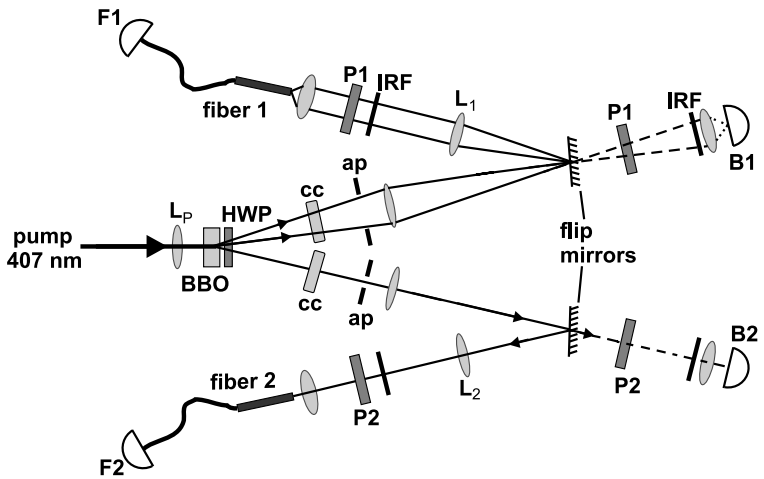

Figure 7.1: *Experimental setup. Lens L_P focuses the pump beam on a birefringent BBO crystal. A half-wave plate HWP and two compensating crystals cc form the standard compensating device. Flip-mirrors allow for an easy switch between two detection schemes. Mirrors flipped up, solid paths: detection with fiber-coupled detectors F_1 and F_2. Lenses L_1 and L_2 are used to direct parallel beams onto the fiber-coupling lenses. Mirrors flipped down, dashed paths: detection with bucket detectors B1 and B2. Both schemes have apertures ap, polarizers P1 and P2, and interference/red filters IRF.*

where we have an one-to-one image of the generating area on the BBO. Flip-mirrors placed at this focus allow for easy switching between our two detection systems. When the mirrors are flipped up, light is directed into 2-m-long single-mode fibers, via imaging lenses and $f = 11$ mm collecting lenses, before being detected by fiber-coupled counting modules (Perkin Elmer SPCM-AQR-14-FC). Spatial selection is now obtained mainly from the fibers, but also somewhat from the extra apertures that are positioned between crystal and flip-mirrors. When the mirrors are flipped down, photons propagate directly to bucket detectors (Perkin Elmer SPCM-AQR-14) and only the mentioned apertures account for spatial selection. In both systems polarizers and interference filters ($\Delta\lambda$ =10 nm) are used for polarization and frequency selection, respectively. A very fast electronic coincidence circuit with a time window of 1.76 ns receives the detector signals and measures the rate of entangled photon pairs.

7.3.2 Mode matching

Detection of SPDC light behind single-mode fibers will generally result in a relatively low yield of entangled photon pairs since the detectors per definition observe only one of the many generated transverse modes. The characterization of the fiber-coupling efficiency in terms of experimental parameters has been studied in [56, 82]. The optimal collection of photon pairs behind single-mode fibers has been experimentally demonstrated by Kurtsiefer *et al.* [23], who showed that transverse matching of the pump mode and the fiber-detected mode is necessary. We will now demonstrate that his discussion of mode matching is incomplete and

Table 7.1: *Measured count rates and visibilities for different geometries of the fiber-detection scheme.*

$w_p(\mu\text{m})$	$w_f(\mu\text{m})$	$R_\text{s}(10^3\text{s}^{-1})$	$R_\text{max}(10^3\text{s}^{-1})$	$V_{45^\circ}(\%)$	$V_{135^\circ}(\%)$
280 ± 10	65 ± 5	10.5	1.53	97.5	99.2
68 ± 2	65 ± 5	247	58.9	98.3	98.4
	33 ± 1	154	20.7	95.3	95.6
30 ± 1	65 ± 5	294	40.9	98.2	97.4
	33 ± 1	223	23.3	95.8	96.5

support this statement with explicit measurements.

According to Kurtsiefer *et al.* [23], mode matching only refers to the matching of the pump waist w_p and the width w_f of the back-traced image of the fiber on the down-conversion crystal: $w_p \approx w_f$. If $w_p > w_f$ near-field losses will occur as some of the produced photon pairs are invisible to the back-traced fiber image. The condition $w_p < w_f$ creates comparable losses as this corresponds to a situation where the angular spread of the SPDC light is certainly larger than the far-field size of the fiber mode. The underlying reason for the joint near-field and far-field match is that the fiber selects a true single transverse mode in both **r**- and **k**-space, in contrast to the mode selection in **r**-space performed by apertures.

The matching condition $w_p \approx w_f$ is not sufficient. Full mode matching requires additional matching to a third spatial parameter, namely the (maximum) internal transverse walk-off w_w between the ordinary and extra-ordinary beam (equivalent to ρL in Sec. 2.2.2), making the full matching condition $w_p \approx w_f \approx w_w$. If $(w_p \approx w_f) < w_w$ the fiber cannot simultaneously match the different near-field profiles of the ordinary and extra-ordinary light. On the other hand, the condition $(w_p \approx w_f) > w_w$ implies a limited observation of the SPDC pattern in the far field, as w_w is Fourier-related to the angular width of the SPDC light [see Eq. (2.6)]. We will now experimentally demonstrate the mode matching of the above three parameters to obtain an optimal yield of photon pairs behind single mode fibers.

Table 7.1 shows the typical single count rates R_s, coincidence count rates R_max and visibilities V that are measured for different geometries in the fiber-detection scheme (aperture fully open at $d = 17$ mm). The pump waist w_p is realized by the choice of the proper pump focusing lens L_p. The two fiber-detected waists $w_f = 33$ μm and $w_f = 65$ μm are obtained with $f = 10$ cm and $f = 20$ cm imaging lenses L_1, respectively (see Fig. 7.1). The transverse walk-off in our 1-mm-thick BBO crystal is $w_w \approx 70$ μm.

In the case of $w_p = 280$ μm and $w_f = 65$ μm, where the pump waist w_p is neither matched to w_f nor to the walk-off w_w, we measure a coincidence rate of $R_\text{max} = 1.53 \times 10^3$ s^{-1}. If we now reduce the pump waist to $w_p = 68$ μm but keep the same w_f, such that all three parameters are matched, we measure an almost 40 times higher rate of $R_\text{max} = 58.9 \times 10^3$ s^{-1}. Table 7.1 obviously shows that a further reduction of the pump waist to $w_p = 30$ μm destroys the complete matching and therefore yields a lower rate of $R_\text{max} = 40.9 \times 10^3$ s^{-1}. If we also

switch to a smaller fiber-detected waist of $w_f = 33\ \mu$m in the latter case, such that again $w_p \approx w_f$, we obtain an even lower coincidence rate of $R_{\max} = 23.3 \times 10^3\ \mathrm{s}^{-1}$. This clearly shows that the matching condition $w_p \approx w_f$ is not sufficient for an optimal collection of photon pairs. Instead, we have hereby demonstrated that a joint matching of all three parameters is needed to obtain the maximal pair rate of $R_{\max} = 58.9 \times 10^3\ \mathrm{s}^{-1}$. Operating at a pump power of 207 mW, this rate corresponds to a slope efficiency of $R_{\max} \times 2 \times 1.7/207 = 970\ \mathrm{s}^{-1}\mathrm{mW}^{-1}$. The factors 2 and 1.7 correct for the use of polarizers and interference filters, respectively (see discussion around Fig. 7.4). Our measured efficiency then compares well to the value of $900\ \mathrm{s}^{-1}\mathrm{mW}^{-1}$ that was obtained by Kurtsiefer *et al.* [23] in absence of both polarizers and interference filters .

7.3.3 Free-space detection versus fiber-coupled detection

Next we compare both the degree of polarization entanglement and the coincidence rate obtained with free-space detection behind apertures on the one hand and with fiber-coupled detectors on the other hand (see Fig. 7.1 for setup). The degree of polarization entanglement can be deduced from the maximum coincidence count rate $R_{\max}$ and the minimum coincidence count rate $R_{\min}$, measured upon rotation of polarizer 2 at fixed orientation φ_1 of polarizer 1. The degree of entanglement is then given by the coincidence fringe visibility

$$V_{\varphi_1} \equiv \frac{R_{\max} - R_{\min}}{R_{\max} + R_{\min}}\ . \tag{7.5}$$

In the natural crystal basis we measure typically $V_{0^\circ} \approx V_{90^\circ} = 99.4 \pm 0.3\%$. Only the visibilities V_{45° and V_{135° are closely related to the experimental implementation of Eq. (7.2) and Eq. (7.4).

Table 7.1 shows a measured visibility of $V = 98.4\%$ for the best-matched geometry of the fiber-detection scheme. In contrast, free-space detection yields only $V = 80.0\%$ under the same conditions ($d = 14$ mm and $w_p = 68\ \mu$m). We can, however, improve the entanglement quality attained with free-space detection to that of the fiber-detection scheme, if we detect behind sufficiently small apertures. For instance, we already measure a visibility of $V = 90.0\%$ behind 9 mm apertures, whereas we even obtain a value of $V = 97.0\%$ behind 4 mm apertures. In Figure 7.2 we show the visibilities V_{45° and V_{135° measured as a function of the aperture diameter d for both detection schemes, using $w_p = 68 \pm 1\ \mu$m and $w_f = 65 \pm 5\ \mu$m. For free-space detection, we clearly observe the "dramatic" increase in visibility with decreasing aperture sizes mentioned above. For fiber-coupled detection, we measure (much) higher visibilities of at least $V = 97.5\%$ for all considered aperture sizes. We ascribe this strong contrast in entanglement quality between the two detection schemes to the removal of spatial labeling by the mode-selective character of the fibers. In fact, the fibers select a pure fundamental transverse mode in both **r** and **k**-space, irrespective of the aperture size, which explains the constantly high visibilities shown in Fig. 7.2. Instead, apertures perform mode selection only in the transverse **r**-space, which leads to enhanced polarization distinguishability and thus lower visibilities for larger apertures.

Unfortunately, the improvement of the entanglement quality for detection behind smaller apertures (see Fig. 7.2) is unavoidably accompanied by a drastic loss of signal strength. Whereas the visibility increases from $V = 80.0\%$ at 17 mm apertures to $V = 90.0\%$ at 9

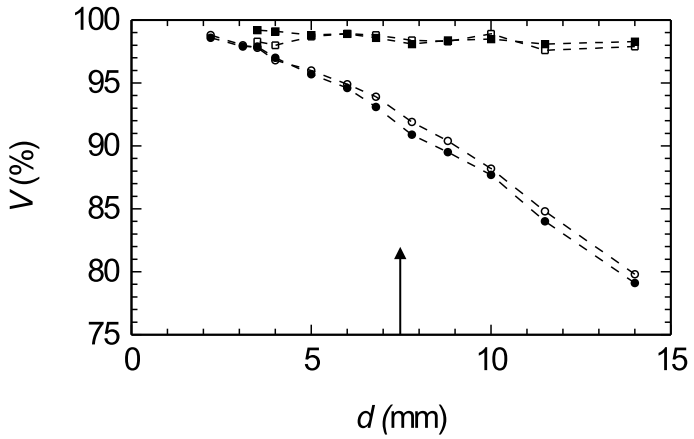

Figure 7.2: *Visibilities V_{45° (filled marks) and V_{135° (open marks) measured as a function of aperture diameter d (at 80 cm from the crystal) for detection behind single-mode fibers (squares) and apertures (circles) at $w_p = 68$ μm and $w_f = 65$ μm. The arrow at $d = 7.5$ mm marks the typical size of the fiber mode in the aperture plane, being the diameter at which the single count rate was reduced to 50% of its maximum value.*

mm apertures and $V = 97.0\%$ at 4 mm apertures, the coincidence rate drops from $R_{\max} = 156 \times 10^3$ s^{-1} to $R_{\max} = 90.0 \times 10^3$ s^{-1} and $R_{\max} = 10.6 \times 10^3$ s^{-1}, respectively. We can enhance the photon yield somewhat, without suffering in the entanglement, by increasing the pump size. For a pump waist of $w_p = 280$ μm instead of $w_p = 68$ μm, we measure a higher rate of $R_{\max} = 33 \times 10^3$ s^{-1} behind 4 mm apertures, thereby obtaining a visibility of $V = 97.7\%$. This improvement in coincidence counts is explained by the smaller SPDC diffraction angle, i.e., the angular spread in one of the two beams that corresponds to a fixed angle in the other beam, as also observed in coincidence imaging [30, 31]. Under this wide-beam condition, free-space detection seems to be favorable above fiber-coupled detection, where we measured only $R_{\max} = 1.53 \times 10^3$ s^{-1} using the same $w_p = 280$ μm. However, the best-matched geometry of the fiber-detection scheme still remains most beneficial as it combines a high visibility of $V = 98.4\%$ with a high coincidence rate of $R_{\max} = 58.9 \times 10^3$ s^{-1} (see Table 7.1).

To summarize, free-space detection is most useful when a large yield of photon pairs is necessary while a high polarization entanglement quality is less crucial. If one wants to improve the degree of entanglement obtained behind apertures, one will inevitably loose some of the generated coincidence pairs. In this respect, we have demonstrated that the best-matched geometry (using $w_p = 68$ μm and $w_f = 65$ μm in our case) in the fiber-coupled detection scheme is most promising when both high entanglement quality and high count rates are accounted for.

7.3.4 Spectral labeling

We will now focus on the limitations to the polarization entanglement that is measured via fiber-coupled detection; these limitations must be attributed to frequency labeling only [see

Eq. (7.3)]. A detailed look at Fig. 7.2 shows that the visibility measured with this scheme is not perfectly 100% and even drops very slightly with increasing aperture sizes. Moreover, we obtain similar visibilities when using 10 m fiber instead of the usual 2 m, which confirms the complete removal of spatial labeling and the presence of spectral labeling only.

Mathematically speaking, the reduction of entanglement quality due to spectral labeling can only be explained by differences between the two projected amplitude functions, i.e., $\alpha_{HV}(\omega_1,\omega_2) \neq \alpha_{VH}(\omega_1,\omega_2)$. As the projected amplitude functions can be written as $\alpha_{ij}(\omega_1,\omega_2) = E_p(\omega_1+\omega_2)\cdot\phi_{ij}(\omega_1,\omega_2)$, the frequency labeling must be contained in the asymmetry of the phase-matching functions, i.e., $\phi_{HV}(\omega_1,\omega_2) \neq \phi_{VH}(\omega_1,\omega_2)$; the spectral pump profile $E_p(\omega_1+\omega_2)$ does not contain any polarization labels. Below we will discuss experimental results that specifically show that phase matching indeed causes the spectral labeling and thus the limited entanglement quality.

First of all, Table 7.1 shows that the visibility decreases from roughly $V = 98\%$ to $V = 96\%$, for both the focusing conditions $w_p = 30$ μm and $w_p = 68$ μm, when the size of the observed pump region is reduced from $w_f = 65$ μm to $w_f = 33$ μm . The reduction in this near-field size corresponds to an increase of the fiber-detected SPDC crossing area in the far field. As a larger observation angle also implies a larger detected spectral bandwidth [23], we will operate further from the thin-crystal limit. In this respect, it is not surprising that the degree of entanglement will suffer even more from the above phase-matching asymmetry.

A second contribution to the spectral labeling could be a (slight) misalignment of the optical fibers. If the fibers are not properly centered around the degeneracy points of the crossing area, the H- and V-polarized spectra will be different because of the frequency matching ($\omega_1+\omega_2=\omega_p$) that is associated with the energy conservation. This again leads to different phase-matching functions ϕ_{HV} and ϕ_{VH} which creates labeling of the two polarizations. Furthermore, even if the fiber alignment is perfect, the degree of entanglement may still suffer from the slightly different bandwidth of the H- and V-polarized light, which we have measured and discussed in Chapter 4 [53].

Intriguingly, we have also observed a limitation of the degree of entanglement due to the power of the pump laser. In Fig. 7.3 we show the visibility measured as a function of the pump power in the fiber-detection scheme, either using $\Delta\lambda$ =10 nm (FWHM) interference filters (dots) or no filters (squares). Here, the apertures are fully open (at $d = 17$ mm), $w_p = 68$ μm and $w_f = 65$ μm. With interference filters we measure visibilities of $V \approx 98\%$ at low pump powers which drop to $V \approx 97\%$ at a power of ≈ 300 mW. When these filters are removed, the reduction from $V \approx 96\%$ to $V \approx 92\%$ in the same power range is more drastic. The observed visibility drop is probably related to a modified pump profile as a result of changes in the temperature and gain guiding in our Kr^+ laser with increased output power. Using a shear interferometer (Melles Griot Wavealyzer) we have observed that an increase in pump power is accompanied by both a larger beam divergence and a transition from a circular to an elliptical cross-section with V/H ratio ≈ 1.2. This modified pump profile changes the biphoton amplitude function Φ_{ij} [see Eq. (7.3)] and thereby its spatially-integrated form $\alpha_{ij}(\omega_1,\omega_2)$ and the corresponding phase-matching function $\phi_{ij}(\omega_1,\omega_2)$. The exact analysis of the observed behaviour in Fig. 7.3 in relation to the beam profile goes beyond the scope of this chapter.

In Fig. 7.4 we show the measured coincidence rates $R_{\max}$ as a function of the pump power, obtained with and without interference filters in the best-matched fiber-detection geometry. In

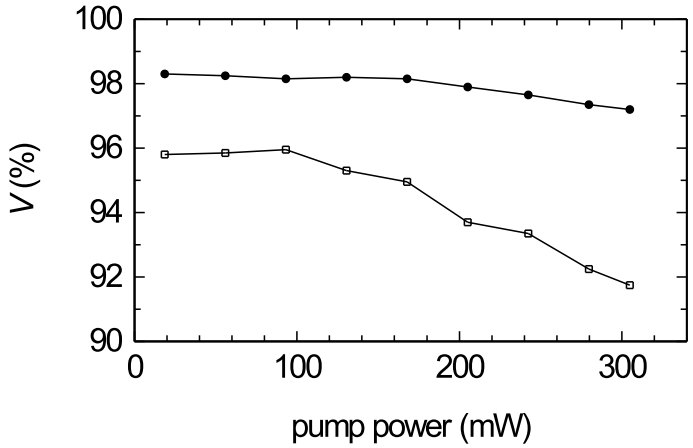

Figure 7.3: *Averaged visibility* $(V_{45^\circ} + V_{135^\circ})/2$ *measured as a function of the pump power, with* $\Delta\lambda = 10$ *nm interference filters (dots) and without interference filters (squares) in the best-matched geometry of the fiber-detection scheme.*

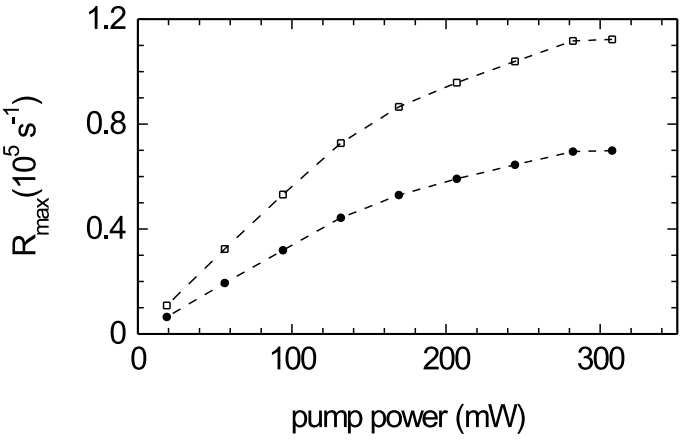

Figure 7.4: *Coincidence rates* $R_{\max}$ *measured as a function of the pump power, with* $\Delta\lambda = 10$ *nm interference filters (dots) and without interference filters (squares) in the best-matched geometry of the fiber-detection scheme.*

absence of the filters we measure 1.7 times higher coincidence rates, which we mainly ascribe to the signal gain of $1/(0.8)^2 = 1.56$ that we calculate from the $T = 80\%$ peak transmission of both filters. The residual gain of 1.7/1.56≈1.1 agrees well with the expected bandwidth increase by a factor of 1.15 which is based on the natural SPDC bandwidth of $\Delta\lambda_{\mathrm{SPDC}} =$ 11.5 nm (see Chapter 4) that we detect without $\Delta\lambda = 10$ nm filters. The smaller detection bandwidth of $\Delta\lambda = 10$ nm, which is associated with less spectral labeling, also explains the somewhat higher visibilities obtained with interference filters (see Fig. 7.3). On the other hand, the fact that $\Delta\lambda$ is just smaller than $\Delta\lambda_{\mathrm{SPDC}}$ indicates that we are not yet operating sufficiently far in the thin-crystal limit and phase matching could thus still limit the attainable

entanglement quality.

Finally, Fig. 7.4 shows a clear saturation of the coincidence rate at higher pump powers, which was also observed by Kurtsiefer *et al.* [23]. This saturation is probably caused by the increased pump divergence mentioned above. As a larger pump divergence implies a larger SPDC diffraction angle, the photon-pair collection within the same aperture will be reduced and saturation will occur. We note that the presented count rates are still low enough to keep saturation effects due to detector deadtimes below the few-percent level.

7.4 Conclusion

We have investigated the limitations to the polarization entanglement in a type-II SPDC setup that employs both free-space detection behind apertures and single-mode detection behind optical fibers. We have demonstrated that optimal photon-pair collection with the latter scheme requires matching to a third parameter, being the birefringent walk-off, apart from the matching of the pump waist and the fiber-detected waist [23]. We ascribe the higher entanglement quality that is measured with the fiber-detection scheme to the erasure of spatial labeling by the single-mode fibers. The remaining spectral labeling comes in essence from imperfect phase matching.